

See discussions, stats, and author profiles for this publication at: <https://www.researchgate.net/publication/251233349>

# Single-Molecule Conductance of Functionalized Oligoynes: Length Dependence and Junction Evolution

ARTICLE in JOURNAL OF THE AMERICAN CHEMICAL SOCIETY · JULY 2013

Impact Factor: 12.11 · DOI: 10.1021/ja4015293 · Source: PubMed

CITATIONS

49

READS

87

11 AUTHORS, INCLUDING:



Wenjing Hong

Xiamen University

36 PUBLICATIONS 1,662 CITATIONS

SEE PROFILE



Veerabhadrarao Kaliginedi

Universität Bern

13 PUBLICATIONS 227 CITATIONS

SEE PROFILE



Colin J Lambert

Lancaster University

314 PUBLICATIONS 4,786 CITATIONS

SEE PROFILE

# Single-Molecule Conductance of Functionalized Oligoynes: Length Dependence and Junction Evolution

Pavel Moreno-García,<sup>†,||,⊥</sup> Murat Gulcur,<sup>‡,⊥</sup> David Zsolt Manrique,<sup>§,⊥</sup> Thomas Pope,<sup>§,⊥</sup> Wenjing Hong,<sup>†</sup> Veerabhadrrao Kaliginedi,<sup>†</sup> Cancan Huang,<sup>†</sup> Andrei S. Batsanov,<sup>‡</sup> Martin R. Bryce,<sup>\*,‡</sup> Colin Lambert,<sup>\*,§</sup> and Thomas Wandlowski<sup>\*,†</sup>

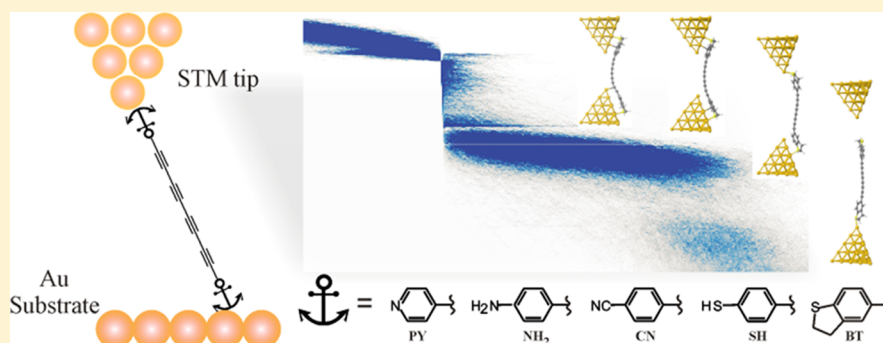
<sup>†</sup>Department of Chemistry and Biochemistry, University of Bern, Freiestrasse 3, CH-3012, Bern, Switzerland

<sup>‡</sup>Department of Chemistry, Durham University, Durham DH1 3LE, United Kingdom

<sup>§</sup>Department of Physics, Lancaster University, Lancaster LA1 4YB, United Kingdom

<sup>||</sup>Instituto de Física, Benemérita Universidad Autónoma de Puebla, Apartado Postal J-48, Puebla 72570, México

## Supporting Information



**ABSTRACT:** We report a combined experimental and theoretical investigation of the length dependence and anchor group dependence of the electrical conductance of a series of oligoynes molecular wires in single-molecule junctions with gold contacts. Experimentally, we focus on the synthesis and properties of diaryl oligoynes with  $n = 1, 2$ , and 4 triple bonds and the anchor dihydrobenzo[*b*]thiophene (BT). For comparison, we also explored the aurophilic anchor group cyano (CN), amino (NH<sub>2</sub>), thiol (SH), and 4-pyridyl (PY). Scanning tunneling microscopy break junction (STM-BJ) and mechanically controllable break junction (MCBJ) techniques are employed to investigate single-molecule conductance characteristics. The BT moiety is superior as compared to traditional anchoring groups investigated so far. BT-terminated oligoynes display a 100% probability of junction formation and possess conductance values which are the highest of the oligoynes studied and, moreover, are higher than other conjugated molecular wires of similar length. Density functional theory (DFT)-based calculations are reported for oligoynes with  $n = 1-4$  triple bonds. Complete conductance traces and conductance distributions are computed for each family of molecules. The sliding of the anchor groups leads to oscillations in both the electrical conductance and the binding energies of the studied molecular wires. In agreement with experimental results, BT-terminated oligoynes are predicted to have a high electrical conductance. The experimental attenuation constants  $\beta_H$  range between  $1.7 \text{ nm}^{-1}$  (CN) and  $3.2 \text{ nm}^{-1}$  (SH) and show the following trend:  $\beta_H(\text{CN}) < \beta_H(\text{NH}_2) < \beta_H(\text{BT}) < \beta_H(\text{PY}) \approx \beta_H(\text{SH})$ . DFT-based calculations yield lower values, which range between  $0.4 \text{ nm}^{-1}$  (CN) and  $2.2 \text{ nm}^{-1}$  (PY).

## INTRODUCTION

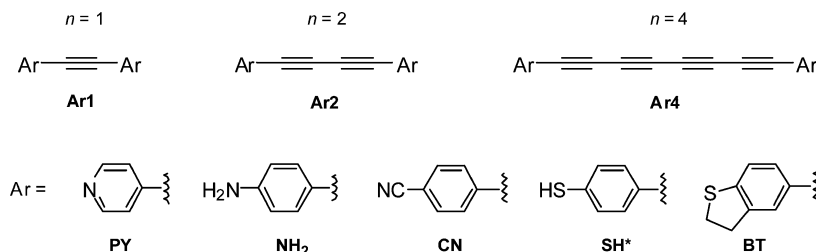
Conjugated polyyne molecules are of interest as a family of carbon-rich backbones.<sup>1-3</sup> They comprise an array of sp-hybridized carbon atoms with alternating single and triple bonds and almost cylindrical electron delocalization in a one-dimensional chain.<sup>2,4,5</sup> Polyynes and shorter sp oligomers (oligoynes) have been proposed for molecular electronics applications (wires, switches, nonlinear optics, etc.).<sup>6,7</sup> Their study is therefore of both fundamental and economic interest. Unlike oligo(phenylenevinylene) (OPV)<sup>8-10</sup> and oligo(phenyleneethynylene) (OPE),<sup>11-14</sup> the conjugation over the oligo/polyyne carbon backbone is not interrupted by phenyl

rings or by bond rotations.<sup>15</sup> Theoretical studies have predicted that polyynes should have excellent intramolecular electron- and charge-transport properties, exhibiting efficient molecular wire behavior.<sup>16-18</sup> In this regard, experimental studies are very much an open issue.

Polyynes possess reduced stability with increasing length of the sp chain. The main strategies to stabilize longer derivatives are to terminate the chains with bulky aryl or organometallic groups<sup>18-21</sup> or to shield the polyyne backbone.<sup>22,23</sup> Without

Received: February 11, 2013

Published: July 22, 2013

Scheme 1. Structures of the Molecules Discussed in This Work and Their Nomenclature<sup>a</sup>

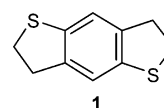
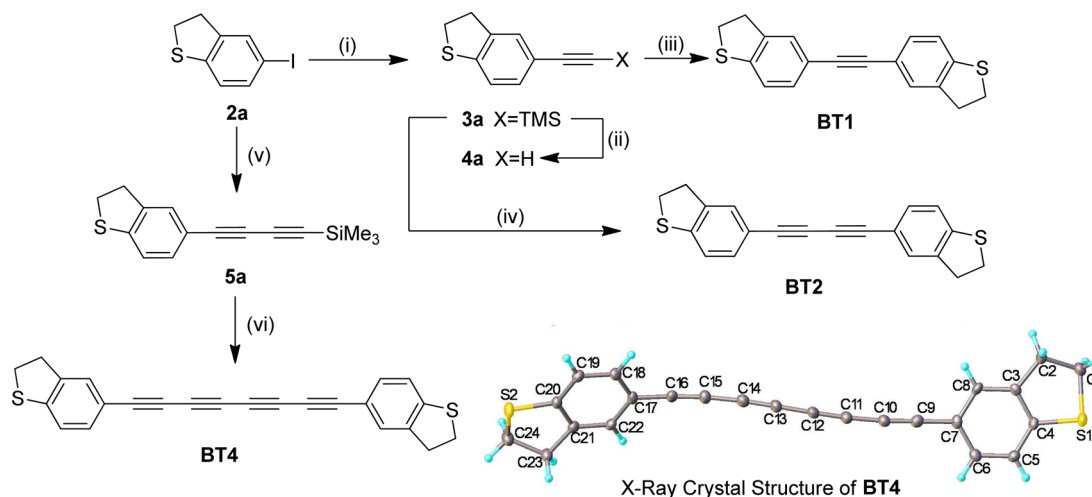
<sup>a</sup>SH1, SH2, and SH4 were isolated as the bis(thioacetate) derivatives.

such stabilizing groups, polyynes which are longer than eight acetylenic carbons (i.e., tetrayne derivatives) tend to decompose or polymerize rapidly at room temperature.<sup>24,25</sup> By using very bulky tris(3,5-di-*t*-butylphenyl)methyl end groups, polyynes comprising up to 44 contiguous carbons have been characterized under normal laboratory conditions.<sup>26</sup> Optical spectroscopic studies in solution showed that these systems exist as alternating single and triple bonds with a very low HOMO–LUMO gap.

A standard protocol for accurately assessing the charge transport through single or a few molecules is to anchor the molecule(s) between metal electrodes (often gold) and to study the electronic properties of the metal–molecule–metal junction by scanning tunneling microscopy (STM) or mechanically controllable break junction (MCBJ) methods.<sup>25–31</sup> This requires molecules to be terminated by functional groups, which have relatively high binding strengths to gold, e.g. thiol,<sup>32,33</sup> pyridyl,<sup>34–36</sup> and amino.<sup>37</sup> However, functional groups at the terminal positions can react (inter- or intramolecularly) with the *sp* backbone to form polymer-like structures,<sup>38</sup> and the bulky terminal groups, which are known to stabilize longer polyynes, are not suitable for anchoring the molecules to metal surfaces. Therefore, it remains a considerable challenge to synthesize oligoynes or polyynes with end-groups which will anchor the molecule to gold (as well as to other conducting leads) and will be stable to purification and handling under ambient conditions. Funda-

mentally new aspects of synthetic oligoyne chemistry need to be developed to enable these  $\pi$ -systems to be exploited in molecular junctions. In this context, the first examples were stable 4-pyridyl (PY) end-capped derivatives up to a C<sub>8</sub> (tetrayne) chain length (PY(–C≡C)<sub>*n*</sub>–PY; *n* = 1, 2, 4). Their electrical properties were studied in STM-BJ experiments.<sup>39</sup> Subsequently a molecule with a C<sub>8</sub> chain between two bulky triarylphosphine–Pt(II) centers bearing thiol end groups was studied in MCBJ experiments.<sup>40</sup> Two very recent papers reported single-molecule charge-transport characteristics of short-chain (*n* = 1) tolane derivatives.<sup>36,41</sup> However, these reports do not address the challenge of the synthesis, characterization, and electrical measurement of longer analogs which is the focus of the present article. We now describe, for the first time, a comprehensive family of diaryl oligoyne molecular wires Ar(–C≡C)<sub>*n*</sub>–Ar, *n* = 1, 2, 4, with five different terminal functionalities (Scheme 1).

We focus on the diaryl oligoynes (*n* = 2, 4) under ambient laboratory conditions. Comparisons are made with the corresponding diarylacetylene (tolane) derivatives (*n* = 1). We explore charge transport characteristics and address the effect of the molecular length on the conductance of these

Scheme 2. Synthesis of BT1, BT2, and BT4<sup>a</sup>

<sup>a</sup>(i) TMSA, [Pd(PPh<sub>3</sub>)<sub>4</sub>], CuI, (*i*-Pr)<sub>2</sub>NH, THF, rt, 4 h, 95%; (ii) TBAF, THF, rt, 15 min, 92%; (iii) 2a, [Pd(PPh<sub>3</sub>)<sub>4</sub>], CuI, (*i*-Pr)<sub>2</sub>NH, THF, rt, 4 h, 75%; (iv) Cu(OAc)<sub>2</sub>·H<sub>2</sub>O, pyridine, MeOH, rt, 12 h, 86%; (v) HC≡C–C≡C–TMS, [Pd(PPh<sub>3</sub>)<sub>4</sub>], (*i*-Pr)<sub>2</sub>NH, THF, rt, 4 h, 78%; (vi) Cu(OAc)<sub>2</sub>·H<sub>2</sub>O, pyridine, MeOH, rt, 12 h, 77%.

families of oligoynes by performing single-molecule transport measurements for the stable derivatives using complementary STM-BJ<sup>34,36</sup> and MCBJ<sup>8,42</sup> techniques. DFT-based calculations provide additional insights into the electronic structure of our molecular junctions. The paper will particularly demonstrate the superior structure and electronic properties of the dihydrobenzo[*b*]thiophene (BT) anchoring group attached to a carbon-rich backbone for charge transport studies in (single) molecular junctions.

## ■ EXPERIMENTAL SECTION

**Synthesis of Diarylloligoynes.** Diarylacetylene (tolane) compounds **Ar1** were synthesized by Sonogashira couplings between the corresponding arylacetylene and aryl iodide derivatives.<sup>43</sup> Compounds **PY2**, **NH<sub>2</sub>2**, and **CN2** derivatives were synthesized by oxidative dimerization of arylacetylenes.<sup>44,45</sup> The diarylbutadiyne derivatives **SH2** [as the bis(thioacetate) derivative], **BT2**, and all diaryltetrayne derivatives **Ar4** were synthesized by dimerization of trimethylsilyl-protected precursor compounds under Eglington–Galbraith coupling conditions [Cu(OAc)<sub>2</sub>·H<sub>2</sub>O, pyridine, methanol] (Scheme SI-1).<sup>44–47</sup> We have also synthesized the BT end-capped compounds **BT1**, **BT2**, and **BT4**, which to our knowledge is the first series of molecules to incorporate this anchor group. The use of this anchor group was motivated by a recent report on the transport properties of compound **1** in metal–molecule–metal junctions.<sup>48</sup>

During the preparation of this manuscript Szafert et al. reported the synthesis of **CN4** using similar methodology.<sup>49</sup>

The reported synthetic route to **1** (by reduction of the parent benzo[1,2-*b*:4,5-*b'*]dithiophene) is not applicable to the functionalized derivatives required for the BT series in the present work, so a new synthetic strategy for functionalization of BT was required. The syntheses of compounds **BT1**, **BT2**, and **BT4** starting from the novel iodo derivative **2a** are shown in Scheme 2.

The diyne derivatives **Ar2** are all stable to storage in air at room temperature. An initial aspect of the work was to establish how the stability of the tetrayne derivatives **Ar4** is dependent on the functionality on the head groups, as this will determine which derivatives are suitable for molecular junction formation. Earlier work showed that primary amines readily react with oligoyne chains<sup>38</sup> and that 2-aminophenyl end-capped tetrayne reacts intramolecularly to form indole derivatives in the presence of a copper salt.<sup>47</sup> We have found that compounds **PY4**, **CN4**, and **BT4** are all very stable under ambient conditions. **NH<sub>2</sub>4** is light sensitive and less stable, which precluded the use of this molecule in junction formation in the present study. Compound **SH4** [bis(thioacetate) derivative] decomposed rapidly, and it could not be purified. However, a UV–vis absorption spectrum of the reaction mixture (Figure S4) showed a significant red shift compared to **SH2**, and the vibronic features are consistent with the formation of the tetrayne **SH4**. The X-ray crystal structures of **CN4**, **BT4**, and **BT2** are discussed in the Supporting Information (SI).

**Conductance Distance Measurements.** The transport properties of single molecular wires were studied using STM-BJ<sup>33,34</sup> and complementary MCBJ<sup>8,42</sup> measurements in solution, at room temperature, and under argon. The STM-BJ approach is based on the repeated formation and breaking of a vertical (single) molecule junction between an atomically sharp gold STM tip and a flat Au(111) substrate, and the simultaneous monitoring of the current  $i_T$  or conductance  $G = i_T/V_{\text{bias}}$  at constant bias voltage  $V_{\text{bias}}$ .<sup>34</sup> The MCBJ technique relies on the formation and rupture of molecular junctions between horizontally suspended gold wires.<sup>42</sup>

The STM-BJ experiments were carried out with a modified Molecular Imaging Pico SPM equipped with a dual-channel preamplifier and housed in an all-glass argon-filled chamber.<sup>13,50</sup> The current ( $i_T$ )–distance ( $\Delta z$ ) measurements were performed with a separate, lab-built analog ramp unit. For further technical details we refer to our previous work.<sup>13,51</sup> The sample electrodes were Au(111) disks, 2 mm height, and 10 mm in diameter or gold single-crystal bead electrodes. The Au(111) substrates were flame annealed before each

experiment. The STM tips were uncoated, electrochemically etched gold wires (Goodfellow, 99.999%, 0.25 mm diameter). The solutions were prepared from 1,3,5-trimethylbenzene (TMB, Aldrich, p.a.) and tetrahydrofuran (THF, Aldrich, p.a.), volume ratio 4:1, containing 0.1 mM of the target molecules. The substrate surface was inspected by STM imaging before the start of each set of  $i_T$ – $\Delta z$  measurements. Typically, we recorded up to 10 000 individual traces with a pulling rate of 58 nm s<sup>−1</sup>.

The MCBJ experiments are based on the trapping of individual molecules between two atomically sharp gold wires (99.999%, Goodfellow, 100  $\mu\text{m}$  diameter), freely suspended and supported on a sheet of spring steel. The latter is bent by a pushing rod, whose vertical movement is controlled by a stepper motor in combination with a piezo stack. The usual moving rate of the pushing rod was 3 to 150 nm s<sup>−1</sup>, which translates into an opening respective closing rate of 0.1–5 nm s<sup>−1</sup>. Typically, we recorded up to 2000 stretching cycles to obtain statistically significant data.

The high mechanical stability of the MCBJ setup allowed also the simultaneous acquisition of current–bias voltage characteristics ( $i_T$ – $V_{\text{bias}}$ ) during the stretching process. We reduced the piezo rate in these experiments to 10 nm s<sup>−1</sup> and swept  $V_{\text{bias}}$  continuously between −1.00 and +1.00 V with 40 V s<sup>−1</sup>. We recorded 500 data points per  $i_T$ – $V_{\text{bias}}$  curve and acquired ca. 25 traces per second. Typically, we measured 20–50 individual curves during the various stages of one single breaking cycle. Further technical details of our MCBJ setup as well as of our measuring routines are described in refs 36 and 42. Finally, we note that the solutions were the same as in the complementary STM measurements.

**Theoretical Methods.** Electronic and transport calculations of the five oligoyne series with BT, SH, PY, NH<sub>2</sub>, CN anchor groups were performed with the *ab initio* code SMEAGOL,<sup>52,53</sup> which uses the Hamiltonian provided by the DFT code SIESTA<sup>54</sup> in combination with the nonequilibrium Green's function formalism. SIESTA employs nonconserving pseudopotentials to account for the core electrons and a linear combination of pseudoatomic orbitals. SMEAGOL divides the entire nanoscale junction into three parts: the left and the right bulk electrodes simulated by multiple gold layers grown along the (111) direction and the “extended molecule” that consists of the molecule and gold pyramids modeling the tip and the electrode. SMEAGOL uses the Hamiltonian derived from SIESTA to calculate self-consistently the density matrix, the transmission coefficients  $T(E)$  of the electrons from the left to the right lead, and the  $i_T$ – $V_{\text{bias}}$  characteristics. Further details about the above computation methods, the energy level alignment, and simulations of the conductance versus distance traces are given in the SI.

## ■ RESULTS AND DISCUSSION

**Dihydrobenzo[*b*]thienyl-capped oligoyne series (BT): Conductance Measurements.** *STM-BJ and MCBJ Conductance Measurements.* Figure 1A displays three typical sample sets of conductance ( $G$ ) versus distance ( $\Delta z$ ) stretching traces, plotted in a semilogarithmic scale, as recorded for the three BT-capped oligoynes **BT1**, **BT2**, and **BT4** in TMB/THF using the STM-BJ approach. After formation of the contact between the gold tip and the Au(111) substrate, the tip was withdrawn with a rate of 58 nm s<sup>−1</sup>. All curves show initially a step-like decrease of the conductance from 10  $G_0$  up to 1  $G_0$ ;  $G_0 = 2e^2/h = 77.5 \mu\text{S}$  being the quantum of conductance. Subsequently, the conductance decreases by several orders in magnitude, which is assigned to the “jump out of contact”.<sup>55</sup> The gold contacts retract suddenly by  $(0.5 \pm 0.1)$  nm, the so-called snap-back distance  $\Delta z_{\text{corr}}$  (see SI and refs 36, 55, and 56 for details). Additional features, such as single and multi conductance plateaus, are observed at  $G \leq G_0$ , which are attributed to the formation of (single) molecular junctions. The noise level is reached at  $G < 10^{-6} G_0$  in the STM-BJ experiments.



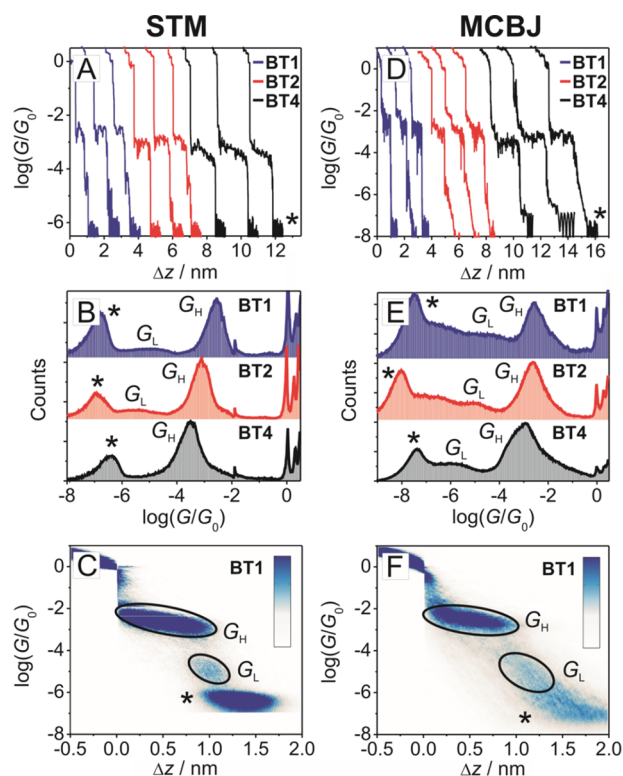


**Figure 1.** Conductance measurements of BT-end-capped oligoynes in TMB/THF (4: 1, v/v) employing a STM-BJ (A–C) and a MCBJ (D–F) setup. (A,D) Typical conductance distance traces of BT1, BT2, and BT4. (B,E) 1D and (C,F) 2D conductance histograms generated from 2000 individual curves. The conductance traces were recorded with  $V_{\text{bias}} = 0.035$  V and a stretching rate of  $58 \text{ nm s}^{-1}$  (STM) or  $5 \text{ nm s}^{-1}$  (MCBJ). The asterisk indicates the noise level of the setup. The small spike at  $\log(G/G_0) \approx -2$  in panel B is an artifact related to the switching of the amplifier stage.

Several thousands of individual  $G$ – $\Delta z$  traces were recorded and subsequently analyzed further by constructing all-data point histograms (without data selection), to extract statistically significant results. Figure 1B displays the corresponding one-dimensional (1D) histograms of BT1, BT2, and BT4 in a semilogarithmic scale. We observe well-defined conductance peaks  $G_H$ , which shift toward lower values with increasing number of  $\text{C}\equiv\text{C}$ – units. Gaussian fits lead to  $(316 \pm 136) \cdot 10^{-5} G_0$ ,  $(81 \pm 9) \cdot 10^{-5} G_0$ , and  $(20 \pm 6) \cdot 10^{-5} G_0$  as most probable conductances of BT1, BT2, and BT4, respectively. We notice that the values of most probable high conductances  $G_H$  were found to be independent of the oligoyne concentration down to 100 nM. Furthermore, the shape of the individual stretching traces, in particular the conductance plateaus in the  $G_H$  region, and the fluctuations of the conductances as well as the most probable characteristic displacement upon junction elongation  $\Delta z_H^*$  (see Figure 2 for definition) do not reveal a significant concentration dependence. Only the probability of junction formation changes with oligoyne concentration due to the limited availability of the target molecules. For further details we refer to SI, Chapter 2.1 (Figure S18), which describes the characteristics of molecular junctions formation of BT1 for concentrations ranging from 1  $\mu\text{M}$  up to 1 mM as a representative case study. These observations provide strong evidence in support of the formation of single molecular junctions under our experimental conditions.

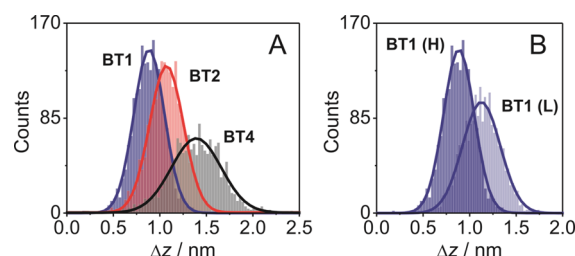


**Figure 2.** (A) Characteristic displacement histograms from STM-BJ experiments as analyzed for BT1, BT2, and BT4 in the high conductance region. (B) Comparison of characteristic displacement histograms of BT1 obtained from the high (H:  $0.7 G_0$ – $3.2 \times 10^{-4} G_0$ ) and in the low (L:  $0.7 G_0$ – $10^{-6} G_0$ ) conductance regions of the 2D conductance versus displacement histograms (Figure 1 and SI).

In addition, BT1 and BT2 revealed a second, rather broad and lower conductance feature  $G_L$  with maxima at  $(0.8 \pm 0.2) \cdot 10^{-5} G_0$  and  $(0.30 \pm 0.03) \cdot 10^{-5} G_0$  for BT concentrations larger than 0.01 mM (Figure S18), respectively. The STM-BJ experiments did not resolve a low conductance  $G_L$  for the longest oligoyne BT4, most probably due to superposition with the noise level.

The above analysis was extended by constructing 2D conductance versus displacement histograms.<sup>51,57</sup> This representation provides direct access to the evolution of molecular junctions during the formation, stretching, and breakdown steps. Figure 1C displays, as a typical example, the data for BT1. (The corresponding plots of BT2 and BT4 are shown in SI.) The individual  $G$ – $\Delta z$  traces were aligned by setting the common origin to  $0.7 G_0$ . The data of Figure 1C reveal quantized conductance features at  $G \geq 1 G_0$ . They correspond to the breaking of gold–gold contacts. Additional high-density data clouds are observed in  $3.3 \times 10^{-4} G_0 \leq G_H \leq 10^{-2} G_0$  and  $10^{-6} G_0 \leq G_L \leq 3.2 \times 10^{-5} G_0$ , centered on  $3.2 \times 10^{-3} G_0$  and  $10^{-5} G_0$ , respectively. These regions represent the high- and the low-conductance states of derivative BT1. The 2D histogram in Figure 1C demonstrates further that both the high and the low conductances decrease monotonously with increasing relative displacement (or junction elongation)  $\Delta z$ .

The results of the STM-BJ experiments are supported by corresponding MCBJ measurements (cf. Figure 1D–F and SI). Table 1 compiles the most probable conductance values of  $G_H^*$  and  $G_L^*$  of the three BT derivatives. The conductances  $G_H$  are significantly higher than reported values of other conjugated molecular wires of similar length.<sup>10,13,58–60</sup> We also note that the higher sensitivity of our MCBJ setup allowed an estimate of the most probable low conductance of BT4, which was obtained as  $G_L^* \approx 0.1 \times 10^{-5} G_0$ .

**Stretching Distance and Junction Formation Probability.** Analyzing the evolution of a molecular junction upon stretching provides additional information about stability and transitions between the two conductance states H and L. We constructed relative displacement ( $\Delta z$ ) histograms<sup>36</sup> by calculating the displacement from the relative zero position at  $0.7 G_0$  ( $G_{\text{max}}$  as upper limit) to the end of the high (low) conductance region of every individual trace. The lower limit  $G_{\text{min}}$  is defined as 1 order of magnitude beneath the most probable high (low) conductances  $G_H^*$  ( $G_L^*$ ) respectively. Both values were obtained from analyzing the 1D histograms (Figure 1).

Figure 2A displays the characteristic displacement histograms of BT1, BT2, and BT4 in the high-conductance region H, and Figure 2B illustrates, as an example, the characteristic

Table 1. Most Probable Conductance Values of Oligoyne (OY) Derivatives As Obtained From STM-BJ and MCBJ Experiments

OY	log( $G/G_0$ ) (STM)			log( $G/G_0$ ) (MCBJ)		JFP <sup>a</sup> %	$\beta$ ( $G_H$ ) <sup>b</sup> nm <sup>-1</sup>	$R_C$ / k $\Omega$
	$G_H$	$G_M$	$G_L$	$G_H$	$G_L$			
PY1	$-3.4 \pm 0.1$	$-4.1 \pm 0.1$	$-5.8 \pm 0.2$	$-3.3 \pm 0.1$	$-5.8 \pm 0.2$	100		
PY2	$-3.76 \pm 0.03$	$-4.5 \pm 0.2$	—	$-3.8 \pm 0.1$	$\sim -7.0$	100	$3.1 \pm 0.4$	$205 \pm 120$
PY4	$-4.4 \pm 0.1$	—	—	—	—	100		
NH <sub>2</sub> 1	$-3.2 \pm 0.1$	—	$-4.8 \pm 0.1$	$-3.2 \pm 0.2$	$-4.8 \pm 0.2$	60	$\sim 2.5$	$\sim 267$
NH <sub>2</sub> 2	$-3.5 \pm 0.1$	—	$-4.9 \pm 0.6$	—	—	95		
CN1	$-4.8 \pm 0.1$	—	—	$-4.7 \pm 0.2$	—	63		
CN2	$-5.0 \pm 0.1$	—	—	$-4.8 \pm 0.2$	—	37	$1.7 \pm 0.1$	$15\,940 \pm 5580$
CN4	$-5.4 \pm 0.1$	—	—	—	—	45		
SH1	$-2.8 \pm 0.1$	—	$-4.56 \pm 0.03$	$-2.7 \pm 0.2$	$-4.7 \pm 0.2$	90	$\sim 3.18$	$\sim 13.5$
SH2	$-3.14 \pm 0.08$	—	$-4.65 \pm 0.05$	$-3.1 \pm 0.2$	—	100		
BT1	$-2.5 \pm 0.2$	—	$-5.1 \pm 0.1$	$-2.5 \pm 0.2$	$-4.9 \pm 0.2$	100		
BT2	$-3.09 \pm 0.05$	—	$-5.52 \pm 0.05$	$-2.6 \pm 0.2$	$-5.3 \pm 0.2$	100	$2.9 \pm 0.2$	$\sim 11 \pm 3$
BT4	$-3.7 \pm 0.1$	—	—	$-3.3 \pm 0.3$	$-6.0 \pm 0.2$	100		

<sup>a</sup>JFP represents the single molecular junction formation probability. <sup>b</sup>The  $\beta$  values were obtained using the average conductance values from STM and MCBJ measurements and the characteristic length  $L_j$  (see Figure 6 for details of the definition of  $L_j$ ). The  $\beta$  values of the NH<sub>2</sub> and SH families are tentative because they are based on measurements of just two derivatives each. The contact resistance  $R_C$  per contact site was obtained from the ordinate intersection at  $L_j = 0$  based on the length dependence of log( $G/G_0$ ) (cf. Figure 4A).

Table 2. Characteristic Lengths of Oligoyne Derivatives and Molecular Junctions As Obtained Experimentally and/or Computed by DFT (see Figure 6 and SI for definitions)

OY	$L_j^a$ nm	$L_j^b$ nm	$L_j^{rel,c}$ nm	$\Delta z_H^*,^d$ nm	$z_H^* = \Delta z_H^* + z_{corr}^e$ nm	$\Delta z_L^*,^d$ nm	$z_L^* = \Delta z_L^* + \Delta z_{corr}^e$ nm	$z_L^* - z_H^*,$ nm
PY1 <sup>f</sup>	0.98	1.40	1.15	$0.56 \pm 0.05$	$1.06 \pm 0.05$	$0.69 \pm 0.05$	$1.19 \pm 0.05$	$0.13 \pm 0.05$
PY2 <sup>f</sup>	1.24	1.66	1.41	$0.68 \pm 0.04$	$1.18 \pm 0.04$	$0.82 \pm 0.05$	$1.32 \pm 0.05$	$0.14 \pm 0.05$
PY4 <sup>f</sup>	1.76	2.18	1.93	$1.45 \pm 0.13$	$1.95 \pm 0.13$	—	—	—
NH <sub>2</sub> 1	1.26	1.74	1.49	$0.68 \pm 0.07$	$1.18 \pm 0.07$	$0.91 \pm 0.10$	$1.41 \pm 0.14$	$0.23 \pm 0.14$
NH <sub>2</sub> 2	1.52	2.00	1.75	$0.82 \pm 0.07$	$1.32 \pm 0.07$	$1.24 \pm 0.02$	$1.74 \pm 0.02$	$0.42 \pm 0.07$
CN1	1.49	1.91	1.66	$0.58 \pm 0.3$	$1.10 \pm 0.3$	—	—	—
CN2	1.76	2.18	1.93	$0.80 \pm 0.12$	$1.30 \pm 0.12$	—	—	—
CN4	2.28	2.70	2.45	$0.67 \pm 0.13$	$1.17 \pm 0.13$	—	—	—
SH1	1.31	1.77	1.52	$0.88 \pm 0.04$	$1.38 \pm 0.04$	$1.26 \pm 0.07$	$1.76 \pm 0.07$	$0.38 \pm 0.07$
SH2	1.57	2.03	1.78	$1.10 \pm 0.09$	$1.60 \pm 0.09$	$1.36 \pm 0.20$	$1.86 \pm 0.19$	$0.26 \pm 0.19$
BT1	1.31	1.79	1.54	$0.88 \pm 0.01$	$1.38 \pm 0.01$	$1.1 \pm 0.2$	$1.62 \pm 0.18$	$0.24 \pm 0.18$
BT2	1.56	2.04	1.79	$1.06 \pm 0.08$	$1.55 \pm 0.08$	$1.3 \pm 0.1$	$1.77 \pm 0.11$	$0.22 \pm 0.11$
BT4	2.08	2.56	2.31	$1.43 \pm 0.10$	$1.93 \pm 0.11$	$1.6 \pm 0.2$	$2.11 \pm 0.16$	$0.18 \pm 0.16$

<sup>a</sup>DFT result for the distance  $L$  from the center of one anchor atom at one end of a fully extended isolated molecule to the center of the anchor atom at the other end. <sup>b</sup> $L_j = L + 0.42$  nm is the maximum possible length of the corresponding junction (see Figure 6 and Table S2). <sup>c</sup> $L_j^{rel} = L_j - 0.25$  nm is the corresponding electrode separation using the same definition of the zero of length used to define  $z_H^*$  and  $z_L^*$ . As shown in Table S2, this is almost identical to the length of a fully extended junction just before breaking, obtained from DFT simulations of junction stretching. <sup>d</sup>Estimated from the experimental relative displacement histograms. <sup>e</sup> $\Delta z_{corr}$  is the snapback distance = 0.5 nm. <sup>f</sup>For the PY series, the data in the  $\Delta z_L^*$  column are for the characteristic length of the middle conductance range  $\Delta z_M^*$ .

displacement histogram of **BT1** extended into the stability range of the low-conductance state L. The data of Figure 2A show uniform normal distributions with well-defined maxima. The maxima correspond to the most probable characteristic distances  $\Delta z^*$ , which are measures of the most-probable plateau lengths of the H conductance states of the three molecules. Gaussian fits to the experimental data revealed the following values of  $\Delta z_H^*$ : ( $0.88 \pm 0.01$ ) nm (**BT1**), ( $1.06 \pm 0.08$ ) nm (**BT2**), and ( $1.43 \pm 0.10$ ) nm (**BT4**), Table 2. The widths of the three distributions appear to increase with molecular length, which suggests larger variations in junction geometry of **BT4** as compared to **BT1**. No stretching trace shorter than 0.5 nm was found, indicating that no direct tunneling traces through the solution were observed.<sup>51</sup> Therefore, we conclude that the molecular junction formation probability in the high-conductance H-state of **BT1**, **BT2**, and **BT4** approaches 100%. Extending the analysis to 0.1  $G_L^*$  reveals a second maximum in the characteristic-displacement

distributions, which is attributed to the most probable characteristic displacement  $\Delta z_L^*$  of the low-conductance state L. Figure 2B shows the corresponding data. We obtained ( $1.1 \pm 0.2$ ) nm, ( $1.3 \pm 0.1$ ) nm, and ( $1.6 \pm 0.2$ ) nm for **BT1**, **BT2**, and **BT4**, respectively (Table 2). Evaluating these data reveals further that all traces transform from the H-state into the L-state upon elongation of the molecular junction before it breaks completely and reaches the noise level.

The most-probable absolute displacements  $z_H^*$  or  $z_L^*$  in an experimental molecular junction formed between a gold STM-tip and an Au(111) surface are obtained by adding the snapback distance  $\Delta z_{corr}$  (cf. refs 36, 55, and 56 and SI) to the relative displacement  $\Delta z$ :  $z_i^* = \Delta z_i^* + \Delta z_{corr}$ ,  $i = H, L$ . Referring to our previous work with short tolane molecules **PY1**, **NH<sub>2</sub>1**, **CN1**, and **SH1**,<sup>36</sup> we used  $\Delta z_{corr} = (0.5 \pm 0.1)$  nm. Table 2 shows a comparison between the resulting values of  $z_H^*$  and  $z_L^*$  and the theoretical estimations of the corresponding electrode displacements of fully extended

junctions just before breaking (denoted  $L_j^{\text{rel}} = L_j - 0.25$  nm in Table 2 and S2). This comparison demonstrates that the experimental values of  $z_H^*$  are typically smaller than the theoretical estimates of  $L_j^{\text{rel}}$ . On the other hand,  $z_L^*$  is significantly larger than  $z_H^*$  and almost equal to  $L_j^{\text{rel}}$ . The relationship between  $L_j^{\text{rel}}$  and a variety of other relevant lengths is addressed in Tables 2 and S2 and Figure 6.

**Conductance Decay and Variation with Displacement.** To gain further insight into the evolution of the molecular conductance upon stretching, we calculated the most probable conductances  $G^{\text{st}}$  at each relative displacement position  $\Delta z$  from Gaussian fits to cross sections of the 2D histograms<sup>37</sup> (Figure 3A). The individual conductance–distance traces,  $G$

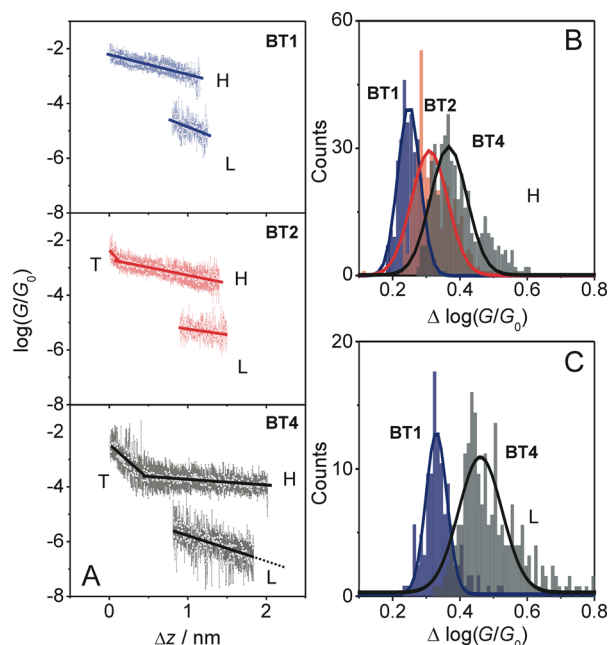


**Figure 3.** (A) Statistically averaged conductance–distance traces (circles) with variation indicated by the standard deviation (bar) and fitting of the traces (line) of BT1, BT2 (STM-BJ), and BT4 (MCBJ). (B) Distribution of variations in conductance  $\Delta \log(G/G_0)$  with reference to the mean values (solid lines in panel A) at different positions in the H conductance and (C) in the L conductance range during stretching of BT1, BT2, and BT4. The data of BT2 nearly coincide with BT1 in panel (C) and are therefore not shown.

versus  $\Delta z$ , and the 2D histograms, such as shown in Figure 1, demonstrate that the plateaus of molecular junctions extend over much longer distances than steps in the Au–Au nanocontacts<sup>36</sup> and that the conductances change during the stretching process by one to two orders in magnitude. These characteristics indicate that there are changes in conformation and contact geometry or aggregation (e.g.,  $\pi$ -stacking, solvation) during the formation and elongation of a molecular junction until rupture. Figure 3A–C displays the statistically averaged conductances versus relative displacement master curves  $\log(G^{\text{st}}/G_0)$  versus  $\Delta z$  together with the standard deviations for BT1, BT2, and BT4 trapped between two gold electrodes in the high- and low-conductance states, respectively.

We observed that  $G^{\text{st}}$  decreases in the high conductance state linearly with slopes of  $0.84$  nm<sup>−1</sup> (BT1),  $0.61$  nm<sup>−1</sup> (BT2), and  $0.31$  nm<sup>−1</sup> (BT4). The slope decreases with molecular length. Compounds BT2 and BT4 show additional regions in  $0 \leq \Delta z \leq 0.11$  and  $0 \leq \Delta z \leq 0.30$  nm, which reflect contributions of

through space tunneling at the beginning of the stretching process and interfere with the molecular junction conductance in these regions. Upon increasing the distance between the gold contacts, the contributions due to direct tunneling decrease, and the slope  $\delta \log(G^{\text{st}}/G_0)/\delta(\Delta z)$  is exclusively determined by the conductance through the molecular junctions. Transition into the low-conductance state L is manifested in the master curve by a coexisting range, which indicates a sequential transition of the molecular junction from H to L, followed by an additional range in the displacement plot that only reveals the L state until rupture.

Changing the oligoyne concentration from 1 mM to 1  $\mu$ M does not lead to modifications of the plot of the statistically averaged most probable conductance  $G^{\text{st}}$  versus the relative displacement position  $\Delta z$ , except that no low-conductance features and a much lower background contribution in the 1D logarithmic histogram were found for BT concentrations below 0.1 mM. These observations strengthen the argument for the formation of single-molecule junctions under our experimental conditions. For the original data and further details we refer to SI, Figure S18.

The distributions of the variation in conductance as shown in Figure 3B and 3C were obtained by decomposing the 2D histograms (Figure 1 and SI) into 1D histograms at different relative displacements  $\Delta z$  and subsequent Gaussian fits.<sup>36</sup> The resulting distributions are rather narrow in displacement regions dominated by the high conductance H-state (Figure 3B), and broaden in the L-state region (Figure 3C). Particularly large fluctuations are observed in the transition region. We also notice that increasing the molecular length  $L$  causes a systematic broadening of variations in the entire displacement region  $\Delta z$ , which clearly indicates a lower stability and less uniform (single) molecular junctions.

**Effect of Molecular Length and Anchoring Group on the Conductance.** We investigated next the influence of molecular length ( $n = 1, 2, 4$ ) and anchoring group on conductance and stability of oligoyne-type molecular junctions following the methodology described above for the three BT-terminated compounds. The key parameters are summarized in Tables 1 and 2. The original experimental data are shown in SI. In the following paragraph we will describe experimental results and correlations, which will be subsequently compared with electronic structure and *ab initio* transport calculations.

**Most Probable Single Junction Conductances.** The PY-terminated oligoynes revealed up to three distinct conductance features upon stretching the molecular junctions,<sup>36,39</sup> which lead to most probable high ( $G_H^*$ ), mid ( $G_M^*$ ) and low ( $G_L^*$ ) conductance values. All three regions were resolved for molecule PY1. We obtained the following results:  $G_H^*(\text{PY1}) = (39 \pm 9) \cdot 10^{-5} G_0$ ,  $G_M^*(\text{PY1}) = (7.9 \pm 2.4) \cdot 10^{-5} G_0$  and  $G_L^*(\text{PY1}) = (0.15 \pm 0.08) \cdot 10^{-5} G_0$ . The data of the high and medium conductance states agree with literature reports<sup>39,61</sup> within half an order of magnitude. In the case of the longer oligoynes, PY2 and PY4, only two and one distinct conductance regions were observed, which leads to  $G_H^*(\text{PY2}) = (17.4 \pm 1.3) \cdot 10^{-5} G_0$ ,  $G_M^*(\text{PY2}) = (3.2 \pm 1.4) \cdot 10^{-5} G_0$  and  $G_H^*(\text{PY4}) = (3.9 \pm 1.1) \cdot 10^{-5} G_0$  (Figure 4, Table 1). No further conductance regions could be resolved for PY2 and PY4 due to limitations in the sensitivity of our setup.

Oligoyne molecular wires end-capped with NH<sub>2</sub>- and SH-anchoring groups demonstrated limited chemical stability for chain lengths  $n > 2$  (see SI). For the shorter members of both families, we found two conductance regions with the most-



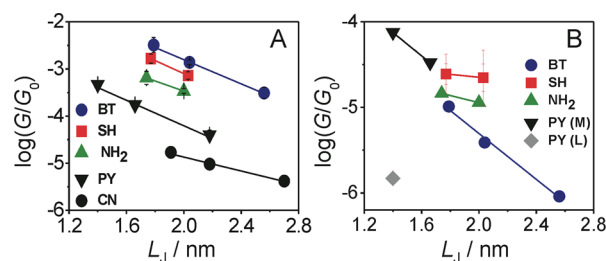


**Figure 4.** Most probable single junction conductance values  $G_H^*$  (A) and  $G_L^*$  (B) of the five families of oligoynes as determined from the analysis of 1D and 2D conductance histograms in dependence on the length parameter  $L_J$  (see Figure 6 and SI for definition).

probable values  $G_H^*$  and  $G_L^*$  shown in Table 1. The high conductance value of the  $\text{NH}_2$ -terminated oligoynes with  $n = 1$  is in good agreement with literature data.<sup>59,62</sup> Published results of the corresponding dithiolate derivatives **SH1**<sup>58</sup> and **SH2**<sup>63</sup> could not be confirmed. Possible reasons might be related to data selection<sup>58,63</sup> or a different experimental geometry intrinsically existing in the  $i_T$  versus time measurements, which is the methodology chosen in ref.<sup>63</sup> Just one region with rather well-defined most probable single junction conductance data  $G_H^*$  was found for the CN-terminated rods **CN1**, **CN2** and **CN4** (Figure 4, Table 1 and SI). The junction formation probability of this family decreases with increasing molecular length.

Figure 4 displays the dependencies of the most probable conductances  $G_H^*$  and  $G_L^*$  versus the characteristic length  $L_J$ .  $L_J$  is the DFT-predicted distance between the centers of the two apex gold atoms in a fully extended molecular junction. The corresponding data are compiled in Table 2. For further details we refer to Figure 6 and the discussion in SI.

The analysis of the most probable high conductance values  $G_H^*$  demonstrates an exponential dependence on distance for oligoynes with PY, CN and BT anchoring groups according to  $G_H^* = G_C \cdot \exp(-\beta_H \cdot L_J)$ .  $G_C$  represents an effective contact conductance reflecting the electronic coupling at the molecule-electrode interface.  $\beta_H$  is the attenuation constant, which characterizes the electronic coupling in a specific molecular backbone in function of its length. The experimentally determined  $\beta_H$  values range between  $(1.7 \pm 0.1) \text{ nm}^{-1}$  (CN) to  $\sim 3.18 \text{ nm}^{-1}$  (SH). The following trend is tentatively observed  $\beta_H(\text{CN}) < \beta_H(\text{NH}_2) < \beta_H(\text{BT}) \approx \beta_H(\text{PY}) < \beta_H(\text{SH})$  (Table 1). We notice that the data set of the  $\text{NH}_2$  and SH-end-capped oligoynes are rather limited. **NH<sub>2</sub>4** and **SH4** could not be measured successfully due to limited stability of these compounds under our experimental conditions. Therefore, the  $\beta$ -values of the  $\text{NH}_2$ - and SH-families should be considered with caution.

The experimental values of the decay parameter  $\beta_H$  of our study compare with those of other molecular bridges as follows: saturated alkanes<sup>10,33,34</sup> ( $7 - 11 \text{ nm}^{-1}$ ) > oligophenyls<sup>64,65</sup> (OP,  $3.5 - 5 \text{ nm}^{-1}$ ) > oligo(phenylene-ethynylenes)<sup>13,58–60</sup> (OPEs,  $2.0 - 3.4 \text{ nm}^{-1}$ ) > oligophenyleimine<sup>66</sup> (OPI,  $3 \text{ nm}^{-1}$ ) > carotenoid polyenes<sup>67,68</sup> ( $1.7 - 2.2 \text{ nm}^{-1}$ ) > oligo(phenylene-vinylenes)<sup>10,69</sup> (OPVs,  $1.7 - 1.8 \text{ nm}^{-1}$ ) > benzene-furan oligoaryls<sup>69</sup> ( $1.1 - 1.3 \text{ nm}^{-1}$ ) > oligothiophenes<sup>70</sup> (OT,  $1.0 \text{ nm}^{-1}$ ) > carbodithioate-capped OPEs<sup>58</sup> (CT,  $0.5 \text{ nm}^{-1}$ ) > porphyrin oligomers<sup>63</sup> ( $0.4 \text{ nm}^{-1}$ ) > pyridyl-capped oligoynes<sup>39</sup> ( $0.06 \text{ nm}^{-1}$ ). Our  $\beta_H$  values are in the same range as those of typical conjugated wires, such as OPEs, OPVs and OPIs. We could not confirm the low  $\beta_H$  values reported by Wang et al. in

a previous study with PY-terminated oligoynes.<sup>39</sup> These conductance data are based on the analysis of  $i_T$  versus time traces in the low bias regime, and differences in the most probable conductances may arise from differences in the statistical treatment of the data and from differences in tip geometries, which affect the position of the Fermi energy relative to the frontier orbitals.

We also observed that the effective contact resistances  $R_C = 1/G_C$ , determined by extrapolating the  $G_H^*$  versus  $L_J$  dependencies toward  $L_J \rightarrow 0$ , lead to the following sequence:  $R_C(\text{BT}) \approx R_C(\text{SH}) < R_C(\text{NH}_2) \approx R_C(\text{PY}) \ll R_C(\text{CN})$  (Table 1). The values of  $\beta_H$  and  $R_C$  demonstrate that the different anchor groups control the strength of the electronic coupling to the metal leads, but also the position of the energy levels involved in the electron transport across the single-molecule junction as well as their coupling into the wire backbone. These aspects will be discussed in detail in the theory section.

Finally, we mention that a decay value of the low conductance region was accessible experimentally only for one molecular family,  $\beta_L(\text{BT}) = (3.1 \pm 0.2) \text{ nm}^{-1}$ . The other oligoynes did not allow the extraction of statistically reliable values. However, at a qualitative level, we may state that the data available for several PY-,  $\text{NH}_2$ -, SH- and BT- molecular wires lead to an effective  $\beta_L$ -value clustering around  $(3.0 \pm 0.5) \text{ nm}^{-1}$ . The absolute values of the corresponding most probable conductances  $G_L^*$  are less dependent on the nature of the anchoring group as compared to  $G_H^*$  (for further details see SI).

The widths of the distribution-variation of the junction conductances at various elongations in the high as well as in the low conductance regions increase in the following order: PY < BT <  $\text{NH}_2$  < SH < CN for oligoynes with  $n = 1$  and  $n = 2$  (Figure 3B and SI). This trend confirms our previous results with tolans ( $n = 1$ ), and is attributed to (i) the simultaneous influence of nonuniform binding geometries (in particular for members of the SH-family) and (ii) a decrease in binding energy/junction stability (CN).<sup>36</sup> The width of the distribution increases also with the molecular length  $L$  within each family, which is particularly attributed to the second factor (Figure 3C and SI). The analysis of the low conductance state results in a larger variation of the respective conductance data (Figure 3C and SI), which correlates with the weaker interaction between the different molecules and a larger variation in possible binding geometries in these junctions. However, the overall trend is the same as that in the high conductance region.

**Stretching Distance and Junction Formation Probability.** Following the strategy outlined for BT-capped oligoynes we constructed relative displacement histograms of all derivatives (SI), and analyzed the characteristic length distributions upon stretching in the high-conductance range, and down to the low-conductance region. We obtained the most probable relative characteristic distances  $\Delta z_i^*$ , the absolute stretching length  $z_i^*$  ( $i = \text{H}, \text{L}$ ) and the junction formation probabilities. These results are summarized in Figure 5 and in Tables 1 and 2.

Analyzing the relative displacement ( $\Delta z_i$ ) distribution allows quantification of the junction formation probability (JFP),<sup>36</sup> e.g., the percentage of successfully created molecular junctions out of all traces recorded (Table 1). These values reach 100% for PY, BT, and SH. Comparing the five molecular families reveals the following trend: CN <  $\text{NH}_2$  < SH  $\approx$  PY  $\approx$  BT. This sequence may be considered as a measure of the stability of the respective junctions. A more detailed analysis of the different breaking pathways indicates that single molecular junctions



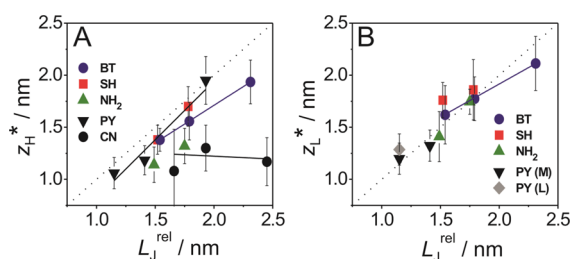


**Figure 5.** Dependence of the most probable characteristic length  $z_i^*$  of molecular junctions,  $i = \text{H,L}$ , on  $L_J^{\text{rel}}$  (see Figure 6 for definition of  $L_J^{\text{rel}}$ ) in the (A) high conductance range  $0.7 G_0 < G < 0.1 G_H$  and in the (B) low conductance range  $0.7 G_0 < G < 0.1 G_L$ . Each data point represents the average value of measurements carried out using at least three different bias values  $V_{\text{bias}}$  (0.025 to 0.170 V). The error bars represent their standard deviations.

with SH, PY, and BT termini break with a high percentage in the low-conductance state, while  $\text{NH}_2$  and CN-terminated wires rupture already upon elongation in the high-conductance region (see SI for details). This trend represents an additional stability marker of the respective molecular junction.

#### DFT Calculations and Analysis of Junction Evolution.

To provide further insight into the experimentally observed trends and the evolution of molecular junctions, we performed theoretical calculations using a combination of DFT and a nonequilibrium Green's function formalism. For each of the molecular families, corresponding to the five distinct anchor groups, each junction was regarded as an "extended molecule" composed of a single molecule attached to two (111) directed pyramids of 35 gold atoms. For a junction geometry such as that shown in Figure 6, we defined the electrode separation  $x_{\text{Au-Au}}$  to be the center-to-center distance between the apex atoms of the two opposing pyramid tips. To generate complete

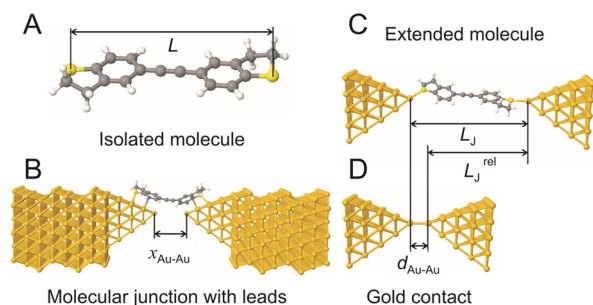


**Figure 6.** Schematic representation of the "extended molecule" of BT1 in contact with conducting leads. This illustrates the relevant distances and lengths  $L$ ,  $x_{\text{Au-Au}}$ ,  $L_J$ ,  $d_{\text{Au-Au}}$ , and  $L_J^{\text{rel}}$ , which were computed after the DFT-based structure has relaxed.  $L$  is the distance from the center of an anchor atom at one end of the fully extended isolated molecule to the center of the anchor atom at the other end. At an arbitrary stage during the theoretical junction stretching, the theoretical electrode separation  $x_{\text{Au-Au}}$  is defined as the distance between the center of the two gold apex atoms.  $L_J$  is defined to be the value of  $x_{\text{Au-Au}}$  when the junction breaks. The distance  $d_{\text{Au-Au}}$  0.25 nm is the electrode separation of a monatomic gold contact, when the junction has the conductance  $G_0$ . This is the gold-gold distance at which the bond between apex atoms is neither compressed nor stretched.  $L_J^{\text{rel}}$  is the theoretically estimated relative displacement of a junction containing a fully extended molecule, arising when the zero of relative displacement ( $\Delta z = 0$ ) corresponds to an apex-atom separation of  $d_{\text{Au-Au}}$  and is defined as  $L_J^{\text{rel}} = L_J - d_{\text{Au-Au}}$  (see Table S2). Panel B shows the structure of the gold electrodes used in the simulations.

pulling curves for each molecule, 50 initial values of electrode separation (denoted  $x_{\text{Au-Au}}^0$ ) were chosen in increments of 0.04 nm, with the shortest distance approximately equal to the molecular length  $L$  minus the thickness of four layers of gold, i.e.,  $\sim L - 1$  nm. For geometry optimization, the first two layers at the base of each pyramid were fixed, and the remaining three layers of each pyramid (closest to the molecule) were allowed to relax. Geometry optimization was carried out using the DFT package SIESTA<sup>53</sup> (for further details see SI). After geometry optimization the electrode separation changed slightly from the initial value  $x_{\text{Au-Au}}^0$  to a final value  $x_{\text{Au-Au}}^*$ .

**Binding Geometry and Binding Energies.** For each initial tip separation  $x_{\text{Au-Au}}^0$ , the molecule was positioned with its anchor rings facing the surface of the pyramids and  $\sim 0.2$  nm away from the local pyramid surface (Figure 6). To avoid artifacts in the geometry optimization due to symmetry, the molecule was initially slightly shifted from the midpoint (0.1 nm) toward one of the electrodes. A selection of these relaxed geometries is shown in Figure 7 for the case of BT4 single-molecule junctions.

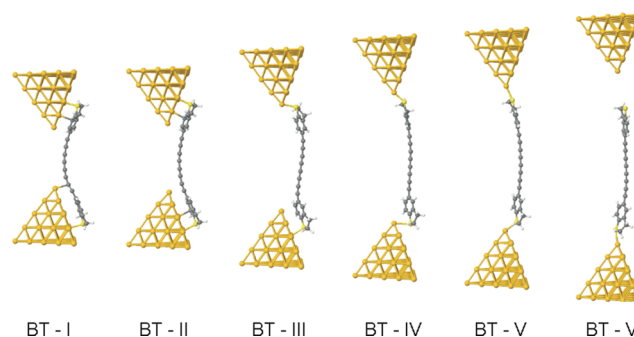


**Figure 7.** Examples of junction evolution of oligoyne derivatives BT4 showing key configurations.

To demonstrate qualitatively the energy changes during the stretching process, we computed the junction energy  $E_J$ , which is defined as the total energy of the relaxed extended molecule (obtained from SIESTA) relative to the total energy of the fully broken junction when the molecule binds only to one of the electrodes (e.g., BT-VI in Figure 7). We investigated 50 different junction geometries for each oligoyne derivative. Figure 8 displays the junction energies for the BT series plotted against the electrode separation. To compare junction energies of molecules with different backbone lengths we define the quantity  $x_n = x_{\text{Au-Au}} - \Delta(n-1)$ , where  $n$  is the number of triple bonds in the molecule and  $\Delta = 0.26$  nm. The latter

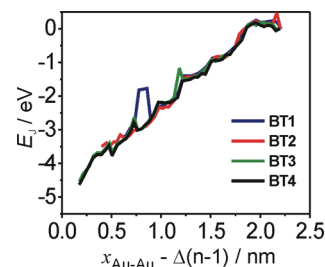


**Figure 8.** Junction energies for the BT series as a function of the scaled electrode separation  $x_n = x_{\text{Au-Au}} - \Delta(n-1)$ , where  $n$  is the number of triple bonds and  $\Delta = 0.26$  nm, the change in length of a molecule when  $n$  increases by unity.

represents the change in length of a molecule when  $n$  increases by unity. Results for the PY, CN, NH<sub>2</sub>, and SH families are shown in Figures S37, S39, S41, and S43.

The fact that the plots of a single family, independent of the molecular length, collapse onto a single curve demonstrates that energies are primarily determined by the anchor group and are only weakly dependent on the length of the oligoyne bridge.

In all cases, as the anchor group slides across the pyramidal tip (SIDE configurations), the junction energy was found to oscillate as a function of  $x_{\text{Au}}$ , with a period which approximately coincides with the gold layer spacing. In an attempt to quantitatively relate to experiments, we computed the binding energies between the molecule and the two gold electrodes using the counterpoise method in the fully broken configuration (e.g., BT-VI shown in Figure 7), denoted as  $E_{\text{b}}^{\text{VI}}$  and in the bridge stage (e.g., BT-V in Figure 7), denoted as  $E_{\text{b}}^{\text{V}}$  (Table 3).

**Table 3. Binding Energies Calculated between a Molecule and Two Electrodes for  $n = 1-4$  Cases for Two Configurations**

(eV)	$n$	BT $n$	PY $n$	SH $n$	CN $n$	NH <sub>2</sub> $n$
$E_{\text{b},1}^{\text{VI}}$	1	0.44	0.40	1.51	0.35	0.37
$E_{\text{b},1}^{\text{V}}$		0.77	0.82	3.00	0.78	0.66
$E_{\text{b},2}^{\text{VI}}$	2	0.44	0.42	1.48	0.34	0.34
$E_{\text{b},2}^{\text{V}}$		0.84	1.12	2.98	0.88	0.66
$E_{\text{b},3}^{\text{VI}}$	3	0.41	0.43	1.47	0.33	0.33
$E_{\text{b},3}^{\text{V}}$		0.78	1.19	3.02	0.94	0.60
$E_{\text{b},4}^{\text{VI}}$	4	0.41	0.41	1.47	0.35	0.33
$E_{\text{b},4}^{\text{V}}$		0.84	1.24	3.13	0.94	0.34
$\bar{E}_{\text{b}}$	—	0.41	0.50	1.51	0.41	0.30

Typically, we find that  $E_{\text{b}}^{\text{VI}}$  is approximately half of  $E_{\text{b}}^{\text{V}}$  because only one of the anchor–gold bond breaks at junction rupture. Across the five anchoring groups we obtained the following trend in the average binding energies  $\bar{E}_{\text{b}}$ : Au–N(NH<sub>2</sub>) < Au–S(BT)  $\approx$  Au–N(CN)  $\approx$  Au–N(PY)  $\ll$  Au–S(SH). The NH<sub>2</sub> anchor binds least strongly, due to steric hindrance caused by the amino group hydrogen atoms. If the binding energies are an indicator of the probability of junction formation, then the above results suggest that BT, PY, and SH should form junctions with a higher probability than NH<sub>2</sub>, in agreement with the experimentally observed low junction formation probability for NH<sub>2</sub>. On the other hand, our experimental findings for the low junction formation probability of CN do not correlate with the theoretically predicted high binding energy of the CN group on gold. This suggests that other factors affect the junction formation, such as competition with solvent molecules and the resilience of an anchor group to defects in the gold leads. Typically we find that the thiol binds with the largest binding energy, although in the calculation we did not cap the molecule with hydrogen after separation from the gold.

**Junction Evolution.** We now describe details of junction evolution, movies of which are presented in the SI. Figure 7 shows snapshots of relaxed geometries for BT4. Geometries for PY4, NH<sub>2</sub>4, CN4, and SH4 are shown in Figure S35. The initial electrode separations  $x_{\text{Au–Au}}^0$  are: 0.62 nm (PY), 0.905 nm (NH<sub>2</sub>), 1.132 nm (CN), 0.968 nm (SH), and 0.956 nm (BT). Initially the carbon atoms at opposite ends of the oligoyne chain tend to bind directly to the tip of the gold pyramids. As shown in Figure 7, BT-I is an exception, for which

no direct bond between the chain and the gold electrodes was found. Upon increasing the separation  $x_{\text{Au–Au}}$ , the molecules undergo a sequence of sliding configurations during the stretching simulation, with the aromatic rings facing the surface of the gold pyramids, as shown in Figures 7 and S35. When the electrode separation  $x_{\text{Au–Au}}$  reaches approximately two-thirds of the molecular length  $L$ , the anchor atom on one side jumps to the top position of one pyramidal gold contact, while the other end of the molecule continues to slide down the gold surface as before. Examples are BT-III (Figure 7) and NH<sub>2</sub>-III, PY-III, CN-III, and SH-III (Figure S35). In some cases, such as PY-IV, CN-IV, and SH-IV (SI, Figure S35), the molecule contorts to bind to atop positions of the gold pyramid. This feature is particularly pronounced for the PY- and CN-end-capped series. As the electrode separation approaches the molecular length  $L$ , the molecules jump into the gap and bind to an apex gold atom of both pyramids (BT-V, PY-V, NH<sub>2</sub>-V, CN-V, SH-V) before the leads are too far apart to bridge, and the junction is broken (BT-VI, PY-VI, NH<sub>2</sub>-VI, CN-VI, SH-VI).

To relate the experimentally measured most-probable breaking lengths,  $z_{\text{i}}^*$ , with the theoretically computed lengths, Table 2 shows the comparison between the experimentally measured lengths  $z_{\text{H}}^*$ ,  $z_{\text{L}}^*$  and the computed length  $L_{\text{J}}^{\text{rel}}$ , where  $L_{\text{J}}^{\text{rel}}$  is the maximum possible length of a junction containing a fully extended molecule. The most probable experimental stretching lengths in the high conductance regime,  $z_{\text{H}}^*$ , are smaller than  $L_{\text{J}}^{\text{rel}}$ , whereas the low-conductance values of  $z_{\text{L}}^*$  are approximately equal to  $L_{\text{J}}^{\text{rel}}$ . The average differences  $z_{\text{L}}^* - z_{\text{H}}^*$  vary between 0.13 nm for PY and up to 0.38 nm for SH and are comparable with the 0.24 nm height of a typical monatomic gold step. Literature reports suggest that strong interactions between contact leads and the anchoring group could cause major rearrangements or even the pulling out of gold atoms.<sup>36,71</sup> The formation of a fully extended molecular junction may also be followed by the creation of intermolecular  $\pi$ -stacking assemblies in the gap.<sup>72,73</sup>

Comparison of  $z_{\text{H}}^*$  with  $L_{\text{J}}^{\text{rel}}$  (Table 2) demonstrates that in the high-conductance regime, none of the oligoyne derivatives assumes a fully stretched molecular junction between the two gold leads. Based on this comparison between  $z_{\text{H}}^*$  and  $L_{\text{J}}^{\text{rel}}$ , we propose that the high-conductance region involves SIDE configuration and multicoordinated sites near the tip of the adjacent gold pyramids. We may distinguish between two groups of oligoyne. The ratio of  $z_{\text{H}}^*/L_{\text{J}}^{\text{rel}}$  is rather high (>90%) for molecular junctions composed of PY-, SH-, and BT-end-capped derivatives indicating stable, slightly tilted (with respect to a fully upright) configurations. The corresponding ratios of NH<sub>2</sub> (<80%) and CN (<65%) derivatives are lower. We also notice that junctions formed by longer molecular wires appear to be less stable than shorter ones as indicated by the lower junction formation probability and a lower ratio  $z_{\text{i}}^*/L_{\text{J}}^{\text{rel}}$ .

Since the values of  $z_{\text{L}}^*$  are comparable with  $L_{\text{J}}^{\text{rel}}$ , we suggest that the experimentally observed low-conductance states represent junction configurations sampled after the “jump” of the anchor atom on one side of the top position of a gold pyramid, while the second atom (anchor group) continues to slide down the gold surface until complete rupture. These regions are depicted by the configurations BT-III (Figure 7) and PY-III and SH-III (Figure S35) and by those samples at larger electrode separations. A low-conductance region was also found for the NH<sub>2</sub>-end-capped oligoyne (Figure 4 and SI), which might indicate that the transition from a SIDE-SIDE into

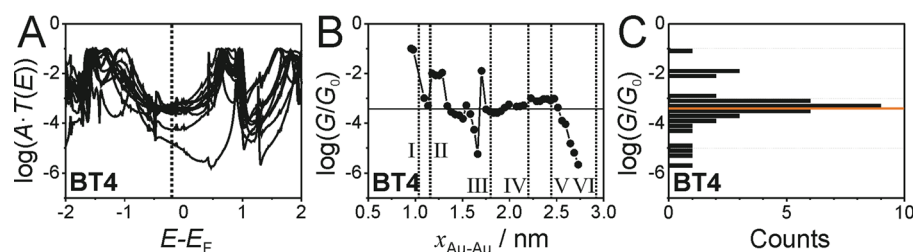


**Figure 9.** (A) Scaled transmission curve  $\log(A \cdot T(E))$  versus  $(E - E_F)$  obtained for BT4 at various stages of the stretching process and (B) the corresponding scaled conductance  $\log(G/G_0)$  versus  $x_{\text{Au-Au}}$  trace (scaling factor 0.10, see text for details). The vertical dotted line in panel (A) marks the shifted Fermi energy  $E_F$ . The thin horizontal line in panel (B) shows the median of the marked conductance points. The roman numeral dotted lines in panel (B) correspond to various geometries shown in Figure 7 (BT-I to BT-VI). Panel (C) shows the histogram generated from data plotted in (B).

an atop-SIDE junction configuration may take place even at an earlier stage of junction elongation.

**Transmission Curves and Single Junction Conductances.** With the above qualitative understanding of junction evolution in end-capped oligynes, we discuss next the theoretical transmission curves and electrical conductances. The underlying DFT mean-field Hamiltonian was used to compute the quantum mechanical electron transmission coefficient  $T(E)$  via the SMEAGOL package. For such transport calculations, the base layers of the pyramids were attached on both sides to eight layers of (111)-oriented bulk gold with each layer consisting of  $6 \times 6$  atoms and a layer spacing of 0.235 nm (Figure 6). These layers were then used to extend the gold electrodes to infinity. Figure 9A shows selected plots of  $T(E)$  versus the energy  $(E - E_F)$  for the BT4. The corresponding plots of  $T(E - E_F)$  versus  $(E - E_F)$  for the entire other families of molecules are shown in Figures S36–S45.

The conductance was then obtained from the electron transmission coefficient  $T(E)$  evaluated at the Fermi energy  $E_F$  multiplied by a scaling factor  $A$  (see below). We note that DFT does not usually predict correctly the alignment of the frontier molecular energy levels in the junction relative to the Fermi energy. To overcome this deficiency, self-energy and screening corrections are required.<sup>55,74,75</sup> However, these corrections are typically obtained for locally optimal configurations in vacuum between rather flat contacts. These conditions do not match our experimental situation (in solution with either one (STM) or two (MCBJ) pyramid-shaped contacts). The correction depends sensitively on the precise coordination of the bridging gold atom, on the relative strengths of binding to the two gold electrodes, and on the position and orientation of the image charges.<sup>75</sup> In view of these uncertainties, we adopted the more empirical approach, which involves computing the  $i_T - V_{\text{bias}}$  characteristics for a range of Fermi energies  $E_F$  in the vicinity of the DFT-predicted Fermi energy  $E_F^{\text{DFT}}$  and adjusting the Fermi energy  $E_F$  so that DFT-SMEAGOL-computed current–voltage characteristics agree with the experimentally measured  $i_T - V_{\text{bias}}$  curves. The method was introduced for tolanes (oligynes with  $n = 1$ ) in ref 36 and is detailed in the SI.

Employing this approach, we estimated the following corrections in  $E_F - E_F^{\text{DFT}}$ : −0.2 eV (BT), −0.65 eV (PY), 0.1 eV (SH), −0.2 eV ( $\text{NH}_2$ ), and −1.0 eV (CN) (see SI for details). To obtain a reasonable fit, it was also necessary to multiply the computed electron transmission coefficient by a single common scaling factor  $A$ , which accounts empirically for the fact that real electrodes contain defects and the well-known deficiencies in DFT. The latter include particularly the absence of van der Waals interactions, which could increase the distance

between the anchors and the gold electrodes and thereby decrease the conductance relative to the generalized-gradient approximation (GGA) values. Comparing experimental and computed data of the five oligoyne families, we obtained  $A = 0.10$  (see also ref 36). This scaling factor is smaller than that in our previous calculations,<sup>36</sup> because we fitted a single scaling parameter to five families of molecules instead of to data from only four individual molecules. Furthermore, we also used an improved model for the electrodes in the present work (Figure 6). For the same reason the corrections in  $E_F$  are slightly modified. The corrections to  $E_F$  indicate that the transport through molecular junctions of PY- and CN-end-capped oligynes is due to nonresonant tunneling through the tails of the respective LUMO states. This is in agreement with results reported for related molecules.<sup>39,51,55</sup> Transport through junctions with SH,  $\text{NH}_2$ , and BT-termini appears to proceed via the tail of the nearby HOMO state, which is also supported by data obtained with similar molecular wires.<sup>48,62,76</sup>

We computed single-molecule junction conductances as a function of the electrode separation  $x_{\text{Au-Au}}$  for the five oligoyne families. The complete set of data including the generated movies illustrating the evolution of the junction configurations and the corresponding transmission functions of the five oligynes is given in the SI.

As an example, Figure 9A displays selected (out of 50) scaled transmission curves of BT4 computed at various stages of the stretching processes. Panel 9B shows the electrical conductances at each electrode separation  $x_{\text{Au-Au}}$  obtained by evaluating the scaled transmission coefficient  $A \cdot T(E - E_F)$  at the Fermi energy  $E = E_F$ . Specific values of  $\log(G/G_0)$  at various stages of the pulling process (Figure 7) are indicated by the vertical dotted lines in Figure 9B. The evolution of the dimensionless junction conductance traces with the electrode separation  $x_{\text{Au-Au}}$  demonstrates that the conductance generally decreases with  $x_{\text{Au-Au}}$  and that the lengths of the plateaus increase with molecular length  $L$  (Figures 9 and S36, S38, S40, S42 and S44). Both trends agree with our experimental observations (Figures 1 and 4 and Table 2, see also SI). A more detailed evaluation of the computed conductance curves suggests that the fluctuations increase upon approaching the transition from SIDE-SIDE to SIDE-atop configurations of the junction (Figure 7), which could be attributed to the characteristic properties of the high and low conductance regions.

The conductance values plotted in Figure 9B were then used to construct conductance histograms (Figure 9C). The most probable conductance values of the high-conductance state  $\log(G/G_0)$  for each family of molecules are plotted as a function of  $L_j$  in Figure 10. The slopes of these curves yield the



computed values  $\beta_{\text{H}}^{\text{comp}}$  (BT) = 1.7 nm<sup>-1</sup>, which is slightly smaller than the experimental values  $\beta_{\text{H}}$ (BT) = (2.9 ± 0.2) nm<sup>-1</sup> (Table 1, Figure 4).

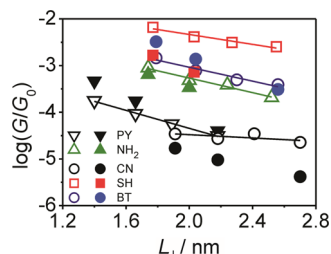


**Figure 10.** Plot of the most probable experimental (full symbols) and computed (open symbols and lines) conductance values  $\log(G/G_0)$  versus the characteristic junction length  $L_j$  for each family of molecules.

The plots of  $\log(G/G_0)$  versus  $L_j$  for the other oligoyne families are shown in Figure 10 and yield the following computed  $\beta_{\text{H}}$  values for the high-conductance regions:  $\beta_{\text{H}}^{\text{comp}}$ (PY) = 2.2 nm<sup>-1</sup>,  $\beta_{\text{H}}^{\text{comp}}$ (NH<sub>2</sub>) = 1.8 nm<sup>-1</sup>,  $\beta_{\text{H}}^{\text{comp}}$ (SH) = 1.2 nm<sup>-1</sup>, and  $\beta_{\text{H}}^{\text{comp}}$ (CN) = 0.4 nm<sup>-1</sup>. The trends in the computed conductances are in qualitative agreement with experimental data, although the theoretical  $\beta_{\text{H}}^{\text{comp}}$  values are consistently smaller than the experimental ones. Within the present theory of phase-coherent tunneling, the latter is a reflection of the well-known tendency for DFT to underestimate the size of the HOMO–LUMO gap, which leads to an underestimation of the decay rate of the transmission coefficient with length. Furthermore, the theoretical calculations were performed in vacuum, whereas the experiments were carried out in the presence of solvent. In the case of NH<sub>2</sub> and thiol-terminated oligoynes differences may also arise, because estimates of  $\beta_{\text{H}}$ (NH<sub>2</sub>) and  $\beta_{\text{H}}$ (SH) are based on only two experimental conductance values ( $n = 1, 2$ ). We also note that the binding energies and transport calculations do not explain the experimentally observed lower stability of the CN-terminated molecular junctions as compared to those with PY anchors.

In contrast with the theoretical pulling curves, which contain rather flat plateaus, the experimental conductance–trace curves tend to decrease during stretching. This difference is likely to arise, because the shape of the tip is unknown and is modeled theoretically as a regular pyramid. In practice, other shapes may arise. The presence of a solvent may also tend to displace the molecule, particularly at longer separations. Furthermore in the simulations, the Fermi energy is assumed to be constant during the pulling process, whereas image charges may cause the HOMO–LUMO gap to increase as the junction length increases, thereby causing the conductance to decay with increasing separation.

Despite these limitations, additional common trends between experiment and simulations were found. The high-conductance plateaus for the BT series (Figures 9B and S44) are flat and less noisy than others (Figures S36, 38, 40, and 42). Furthermore, Figure S40 shows that the plateaus of the PY series are steeper than all others. The SH derivatives shown in Figure S42 represent an exception, because the tail of the conductance plateaus increases as the molecular wire approaches breaking (see SI), whereas the experimental 2D conductance displacement histograms show a decreasing trend with the low-conductance state at the end. This difference arises because in

the simulations, as the molecule detaches from the electrodes, the sulfur termini become thiyl free radicals, which leads to the alignment of the HOMO resonance with  $E_{\text{F}}$ . In contrast, the radical species is not isolated under experimental conditions but surrounded by an environmental reservoir, which neutralizes excess charges and/or free radicals, respectively.<sup>77</sup>

To shed further light on the origin of the low-conductance states, we compare the results of the computed scaled conductances  $\log(G/G_0)$  versus  $x_{\text{Au–Au}}$  traces (Figures 9 and S36, S38, S40, S42 and S44) with the values of  $z_{\text{L}}^*$ , the experimentally observed most probable absolute displacements in the low-conductance regions (Table 2). Both values are related to each other according to  $x_{\text{Au–Au}} = z_{\text{L}}^* + 0.25$  nm. With this correspondence, we note that the experimental values of ( $z_{\text{L}}^* + 0.25$ ) of the four families BT, PY, SH, and NH<sub>2</sub> coincide with the ends of the plateaus and the beginning of the regions of low conductances in the computed conductance traces (Figure 9 and S36, S38, S40, S42 and S44). From the movies provided in the SI, the ends of the plateaus correspond to anchor groups binding to the top atoms of the pyramidal contacts. Therefore this is one possible contribution to the measured low conductances. However since low conductances are measured also at separations greater than the most probable value  $z_{\text{L}}^*$  these cannot be single-molecule configurations unless an Au atom is pulled from the contact. Alternatively, such low-conductance states could arise from the  $\pi$ – $\pi$  stacking of two or more molecules, with one molecule bound to the lower contact and the other bound to the upper contact.

## CONCLUSIONS

By using rational molecular design and synthesis, combined with STM-BJ and MCBJ techniques, we have comprehensively studied diarylloigoynes terminated with the novel anchor group BT for the attachment to gold electrodes. Comparative studies were also carried out with CN, NH<sub>2</sub>, SH, and PY anchors. We find that the shorter  $n = 1$  (tolane) and  $n = 2$  (butadiyne) molecules are all stable under ambient conditions. For the  $n = 4$  (tetrayne) analogs, the CN, pyridyl, and BT derivatives are stable; however, the NH<sub>2</sub> and SH derivatives rapidly decompose at room temperature, presumably due to the terminal groups reacting intermolecularly with the oligoyne backbone. Overall, our joint experimental and theoretical investigations of the length dependence and anchor-group dependence suggest that BT-terminated oligoynes are particularly attractive: They display the highest probability of junction formation and electrical conductance values which are higher than reported values of other conjugated molecular wires of similar length. Based on concentration-dependent studies of the target molecules between 100 nM and 1 mM, we provide convincing evidence for the formation of single-molecule junctions in the high-conductance state under our experimental conditions. The low-conductance state is attributed to two possible scenarios: (i) single-molecule junctions involving the pulling out of gold atoms from the contact leads or (ii) multimolecular junctions involving  $\pi$ – $\pi$  stacking.

Comparable experimental results were obtained using STM-BJ and MCBJ setups, especially for the high-conductance states: the experimental  $\beta_{\text{H}}$  values range between 1.7 nm<sup>-1</sup> (CN) to 3.2 nm<sup>-1</sup> (SH), with the following tentative trend  $\beta_{\text{H}}$ (CN) <  $\beta_{\text{H}}$ (NH<sub>2</sub>) <  $\beta_{\text{H}}$ (BT)  $\approx$   $\beta_{\text{H}}$ (PY)  $\approx$   $\beta_{\text{H}}$ (SH). Theoretical values were lower, in the range of 0.4–2.2 nm<sup>-1</sup>, with  $\beta_{\text{H}}^{\text{comp}}$ (CN) <  $\beta_{\text{H}}^{\text{comp}}$ (SH) <  $\beta_{\text{H}}^{\text{comp}}$ (NH<sub>2</sub>)  $\approx$   $\beta_{\text{H}}^{\text{comp}}$ (BT)  $\approx$   $\beta_{\text{H}}^{\text{comp}}$ (PY). To compare with experiments, we calculated whole conductance–



trace curves, whose evolution with electrode separation is demonstrated for each molecular family in full movies. We show further that the sliding of the anchor groups across the pyramidal gold electrodes leads to oscillations in both the electrical conductance and the junction energies of the molecular wires. These conductance traces were used to generate conductance histograms, which compare favorably with the high-conductance regions of the experimental histograms obtained from STM-BJ and MCBJ measurements.

To summarize, this study has shown that stable oligoynes with up to eight acetylenic carbons in the backbone (i.e., tetraynes) can be synthesized with different end groups that are suitable for anchoring the molecules to gold electrodes. BT anchor groups are shown to be particularly beneficial in this regard. Oligoynes are now established as a versatile class of  $\pi$ -conjugated molecular wires for the fabrication of highly conductive nanoscale junctions.

## ■ ASSOCIATED CONTENT

### ■ Supporting Information

Experimental part: synthesis and characterization of oligoynes compounds, UV–vis absorption and NMR spectra, X-ray crystallography, stability tests, transport measurements and data analysis procedures, conductance dependence on concentration. Computational part: simulation for isolated molecules, length scale, electrical conductance and transmission curves of molecules within junctions, movies of junction evolution. This material is available free of charge via the Internet at <http://pubs.acs.org>.

## ■ AUTHOR INFORMATION

### Corresponding Author

c.lambert@lancaster.ac.uk; m.r.bryce@durham.ac.uk; thomas.wandlowski@dcb.unibe.ch

### Author Contributions

<sup>†</sup>These authors contributed equally.

### Notes

The authors declare no competing financial interest.

## ■ ACKNOWLEDGMENTS

This work was generously supported by the Swiss National Science Foundation (200021-124643; NFP 62), the German Science Foundation (priority program SPP 1243), the UK EPSRC, the EC FP7 ITN “FUNMOLS” project no. 212942, and the University of Bern. P.M.G. also acknowledges support from CONACyT, México (209297).

## ■ REFERENCES

- (1) *Acetylene Chemistry: Chemistry, Biology and Material Science*; Diederich, F., Stang, P. J., Tykwinski, R. R., Eds.; Wiley-VCH: Weinheim: Germany, 2005.
- (2) Nielsen, M. B.; Diederich, F. *Chem. Rev.* **2005**, *105*, 1837–1868.
- (3) Gholami, M.; Tykwinski, R. R. *Chem. Rev.* **2006**, *106*, 4997–5027.
- (4) *Carbon-Rich Compounds: From Molecules to Materials*; Haley, M. L., Tykwinski, R. R., Eds.; Wiley-VCH: Weinheim, Germany, 2006.
- (5) Szafert, S.; Gladysz, J. A. *Chem. Rev.* **2003**, *103*, 4175–4206.
- (6) Slepko, A. D.; Hegmann, F. A.; Eisler, S.; Elliott, E.; Tykwinski, R. R. *J. Chem. Phys.* **2004**, *120*, 6807–6810.
- (7) Cornil, J.; Beljonne, D.; Calbert, J. P.; Brédas, J. L. *Adv. Mater.* **2001**, *13*, 1053–1067.
- (8) Huber, R.; Gonzalez, M. T.; Wu, S.; Langer, M.; Grunder, S.; Horhoiu, V.; Mayor, M.; Bryce, M. R.; Wang, C. S.; Jitchati, R.

Schonenberger, C.; Calame, M. *J. Am. Chem. Soc.* **2008**, *130*, 1080–1084.

(9) Newton, M. D.; Smalley, J. F. *Phys. Chem. Chem. Phys.* **2007**, *9*, 555–572.

(10) Liu, H. M.; Wang, N.; Zhao, J. W.; Guo, Y.; Yin, X.; Boey, F. Y. C.; Zhang, H. *ChemPhysChem* **2008**, *9*, 1416–1424.

(11) Taylor, J.; Brandbyge, M.; Stokbro, K. *Phys. Rev. B* **2003**, *68*, 121101.

(12) James, D. K.; Tour, J. M. *Chem. Mater.* **2004**, *16*, 4423–4435.

(13) Kaliginedi, V.; Moreno-García, P.; Valkenier, H.; Hong, W.; García-Suárez, V. M.; Buiterr, P.; Otten, J. L. H.; Hummelen, J. C.; Lambert, C. J.; Wandlowski, T. *J. Am. Chem. Soc.* **2012**, *134*, 5262–5275.

(14) Tour, J. M. *Acc. Chem. Res.* **2000**, *33*, 791–804.

(15) Finch, C. M.; Sirichantaropass, S.; Bailey, S. W.; Grace, I. M.; Garcia-Suarez, V. M.; Lambert, C. J. *J. Phys.: Condens. Matter* **2008**, *20*, 022203.

(16) Crljen, Ž.; Baranović, G. *Phys. Rev. Lett.* **2007**, *98*, 116801.

(17) Garcia-Suarez, V. M.; Lambert, C. J. *Nanotechnology* **2008**, *19*, 455203.

(18) Gbitter, T.; Hampel, F.; Gisselbrecht, J.-P.; Hirsch, A. *Chem.—Eur. J.* **2002**, *8*, 408–432.

(19) Luu, T.; Elliott, E.; Slepko, A. D.; Eisler, S.; McDonald, R.; Hegmann, F. A.; Tykwinski, R. R. *Org. Lett.* **2004**, *7*, 51–54.

(20) Mohr, W.; Stahl, J.; Hampel, F.; Gladysz, J. A. *Chem.—Eur. J.* **2003**, *9*, 3324–3340.

(21) Wang, C.; Batsanov, A. S.; West, K.; Bryce, M. R. *Org. Lett.* **2008**, *10*, 3069–3072.

(22) Klinger, C.; Vostrowsky, O.; Hirsch, A. *Eur. J. Org. Chem.* **2006**, 1508–1524.

(23) Sugiyama, J.; Tomita, I. *Eur. J. Org. Chem.* **2007**, *2007*, 4651–4653.

(24) Johnson, T. R.; Walton, D. R. M. *Tetrahedron* **1972**, *28*, 5221–5236.

(25) Simpkins, S. M. E.; Weller, M. D.; Cox, L. R. *Chem. Commun.* **2007**, 4035–4037.

(26) Chalifoux, W. A.; Tykwinski, R. R. *Nat. Chem.* **2010**, *2*, 967–971.

(27) Chen, F.; Hihath, J.; Huang, Z. F.; Li, X. L.; Tao, N. J. *Annu. Rev. Phys. Chem.* **2007**, *58*, 535–564.

(28) Akkerman, H. B.; de Boer, B. J. *Phys.: Cond. Matt* **2008**, *20*, 013001.

(29) McCreery, R. L.; Bergren, A. J. *Adv. Mater.* **2009**, *21*, 4303–4322.

(30) Cuevas, J. C.; Scheer, E. *Molecular Electronics: An Introduction to Theory and Experiment*; World Scientific Series in Nanoscience and Nanotechnology; World Scientific: Singapore, 2010.

(31) *Unimolecular and Supramolecular Electronics I in Topics in Current Chemistry*; Metzger, R. M. Ed.; Springer: New York, 2012.

(32) Chen, F.; Li, X. L.; Hihath, J.; Huang, Z. F.; Tao, N. J. *J. Am. Chem. Soc.* **2006**, *128*, 15874–15881.

(33) Li, C.; Pobelov, I.; Wandlowski, T.; Bagrets, A.; Arnold, A.; Evers, F. *J. Am. Chem. Soc.* **2008**, *130*, 318–326.

(34) Xu, B. Q.; Tao, N. J. *J. Science* **2003**, *301*, 1221–1223.

(35) Kamenetska, M.; Quek, S. Y.; Whalley, A. C.; Steigerwald, M. L.; Choi, H. J.; Louie, S. G.; Nuckolls, C.; Hybertsen, M. S.; Neaton, J. B.; Venkataraman, L. *J. Am. Chem. Soc.* **2010**, *132*, 6817–6821.

(36) Hong, W.; Manrique, D. Z.; Moreno-García, P.; Gulcur, M.; Mishchenko, A.; Lambert, C. J.; Bryce, M. R.; Wandlowski, T. *J. Am. Chem. Soc.* **2012**, *134*, 2292–2304.

(37) Venkataraman, L.; Klare, J. E.; Tam, I. W.; Nuckolls, C.; Hybertsen, M. S.; Steigerwald, M. L. *Nano Lett.* **2006**, *6*, 458–462.

(38) Ziessel, R.; Suffert, J.; Youinou, M.-T. *J. Org. Chem.* **1996**, *61*, 6535–6546.

(39) Wang, C. S.; Batsanov, A. S.; Bryce, M. R.; Martin, S.; Nichols, R. J.; Higgins, S. J.; Garcia-Suarez, V. M.; Lambert, C. J. *J. Am. Chem. Soc.* **2009**, *131*, 15647–15654.

(40) Ballmann, S.; Hieringer, W.; Secker, D.; Zheng, Q.; Gladysz, J. A.; Görling, A.; Weber, H. B. *ChemPhysChem* **2010**, *11*, 2256–2260.

- (41) Zotti, L. A.; Kirchner, T.; Cuevas, J. C.; Pauly, F.; Huhn, T.; Scheer, E.; Erbe, A. *Small* **2010**, *6*, 1529–1535.
- (42) Hong, W.; Valkenier, H.; Mészáros, G.; Manrique, D. Z.; Mishchenko, A.; Putz, A.; García, P. M.; Lambert, C. J.; Hummelen, J. C.; Wandlowski, T. *Beilstein J. Nanotechnol.* **2011**, *2*, 699–713.
- (43) *Metal-Catalysed Cross-Coupling Reactions*; de Meijere, A., Diederich, F., Ed.; Wiley-VCH: Weinheim, Germany, 2004.
- (44) Siemsen, P.; Livingston, R. C.; Diederich, F. *Angew. Chem., Int. Ed.* **2000**, *39*, 2632–2657.
- (45) Rossi, R.; Carpita, A.; Bigelli, C. *Tetrahedron Lett.* **1985**, *26*, 523–526.
- (46) Eglinton, G.; Galbraith, A. R. *Chem. Ind. (London)* **1956**, 737–738.
- (47) Fiandanese, V.; Bottalico, D.; Marchese, G.; Punzi, A. *Tetrahedron* **2008**, *64*, 53–60.
- (48) Park, Y. S.; Widawsky, J. R.; Kamenetska, M.; Steigerwald, M. L.; Hybertsen, M. S.; Nuckolls, C.; Venkataraman, L. *J. Am. Chem. Soc.* **2009**, *131*, 10820–10821.
- (49) Gulia, N.; Osowska, K.; Pigulski, B.; Lis, T.; Galewski, Z.; Szafert, S. *Eur. J. Org. Chem.* **2012**, 4819–4830.
- (50) Meszaros, G.; Li, C.; Pobelov, I.; Wandlowski, T. *Nanotechnology* **2007**, *18*, 424004.
- (51) Mishchenko, A.; Zotti, L. A.; Vonlanthen, D.; Burkle, M.; Pauly, F.; Cuevas, J. C.; Mayor, M.; Wandlowski, T. *J. Am. Chem. Soc.* **2011**, *133*, 184–187.
- (52) Rocha, A. R.; Garcia-Suarez, V. M.; Bailey, S.; Lambert, C.; Ferrer, J.; Sanvito, S. *Phys. Rev. B* **2006**, *73*, 085414.
- (53) Rocha, A. R.; Garcia-Suarez, V. M.; Bailey, S. W.; Lambert, C. J.; Ferrer, J.; Sanvito, S. *Nat. Mater.* **2005**, *4*, 335–339.
- (54) Soler, J. M.; Artacho, E.; Gale, J. D.; Garcia, A.; Junquera, J.; Ordejon, P.; Sanchez-Portal, D. *J. Phys.: Condens. Matter* **2002**, *14*, 2745.
- (55) Quek, S. Y.; Kamenetska, M.; Steigerwald, M. L.; Choi, H. J.; Louie, S. G.; Hybertsen, M. S.; Neaton, J. B.; Venkataraman, L. *Nat. Nanotechnol.* **2009**, *4*, 230–234.
- (56) Yanson, A. I.; Bollinger, G. R.; van den Brom, H. E.; Agrait, N.; van Ruitenbeek, J. M. *Nature* **1998**, *395*, 783–785.
- (57) Martin, C. A.; Ding, D.; Sorensen, J. K.; Bjornholm, T.; van Ruitenbeek, J. M.; van der Zant, H. S. J. *J. Am. Chem. Soc.* **2008**, *130*, 13198–13199.
- (58) Xing, Y. J.; Park, T. H.; Venkatramani, R.; Keinan, S.; Beratan, D. N.; Therien, M. J.; Borguet, E. *J. Am. Chem. Soc.* **2010**, *132*, 7946–7956.
- (59) Lu, Q.; Liu, K.; Zhang, H. M.; Du, Z. B.; Wang, X. H.; Wang, F. *ACS Nano* **2009**, *3*, 3861–3868.
- (60) Liu, K.; Li, G.; Wang, X.; Wang, F. *J. Phys. Chem. C* **2008**, *112*, 4342–4349.
- (61) Velizhanin, K. A.; Zeidan, T. A.; Alabugin, I. V.; Smirnov, S. J. *Phys. Chem. B* **2009**, *114*, 14189–14193.
- (62) Hybertsen, M. S.; Venkataraman, L.; Klare, J. E.; Whalley, A. C.; Steigerwald, M. L.; Nuckolls, C. *J. Phys.: Condens. Matter* **2008**, *20*, 374115.
- (63) Sedghi, G.; Sawada, K.; Esdaile, L. J.; Hoffmann, M.; Anderson, H. L.; Bethell, D.; Haiss, W.; Higgins, S. J.; Nichols, R. J. *J. Am. Chem. Soc.* **2008**, *130*, 8582–8583.
- (64) Wold, D. J.; Haag, R.; Rampi, M. A.; Frisbie, C. D. *J. Phys. Chem. B* **2002**, *106*, 2813–2816.
- (65) Ishida, T.; Mizutani, W.; Aya, Y.; Ogiso, H.; Sasaki, S.; Tokumoto, H. *J. Phys. Chem. B* **2002**, *106*, 5886–5892.
- (66) Choi, S. H.; Kim, B.; Frisbie, C. D. *Science* **2008**, *320*, 1482–1486.
- (67) He, J.; Chen, F.; Li, J.; Sankey, O. F.; Terazono, Y.; Herrero, C.; Gust, D.; Moore, T. A.; Moore, A. L.; Lindsay, S. M. *J. Am. Chem. Soc.* **2005**, *127*, 1384–1385.
- (68) Visoly-Fisher, I.; Daie, K.; Terazono, Y.; Herrero, C.; Fungo, F.; Otero, L.; Durantini, E.; Silber, J. J.; Sereno, L.; Gust, D.; Moore, T. A.; Moore, A. L.; Lindsay, S. M. *Proc. Natl. Acad. Sci. U.S.A.* **2006**, *103*, 8686–8690.
- (69) Chen, I. W. P.; Fu, M.-D.; Tseng, W.-H.; Chen, C.-h.; Chou, C.-M.; Luh, T.-Y. *Chem. Commun.* **2007**, 3074–3076.
- (70) Yamada, R.; Kumazawa, H.; Noutoshi, T.; Tanaka, S.; Tada, H. *Nano Lett.* **2008**, *8*, 1237–1240.
- (71) Paulsson, M.; Krag, C.; Frederiksen, T.; Brandbyge, M. *Nano Lett.* **2009**, *9*, 117–121.
- (72) Wu, S. M.; Gonzalez, M. T.; Huber, R.; Grunder, S.; Mayor, M.; Schonenberger, C.; Calame, M. *Nat. Nanotechnol.* **2008**, *3*, 569–574.
- (73) Martin, S.; Grace, I.; Bryce, M. R.; Wang, C. S.; Jitchati, R.; Batsanov, A. S.; Higgins, S. J.; Lambert, C. J.; Nichols, R. J. *J. Am. Chem. Soc.* **2010**, *132*, 9157–9164.
- (74) Mowbray, D. J.; Jones, G.; Thygesen, K. S. *J. Chem. Phys.* **2008**, *128*, 111103–5.
- (75) Dell'Angela, M.; Kladnik, G.; Cossaro, A.; Verdini, A.; Kamenetska, M.; Tamblyn, I.; Quek, S. Y.; Neaton, J. B.; Cvetko, D.; Morgante, A.; Venkataraman, L. *Nano Lett.* **2010**, *10*, 2470–2474.
- (76) Bratkovsky, A. M.; Kornilovitch, P. E. *Phys. Rev. B* **2003**, *67*, 115307.
- (77) Bruot, C.; Hihath, J.; Tao, N. *Nat. Nanotechnol.* **2012**, *7*, 35–40.